

Understanding the Formation of Antiphase Boundaries in Layered Oxide Cathode Materials and Their Evolution upon Electrochemical Cycling

Shamail Ahmed,¹ Anuj Pokle,¹ Matteo Bianchini,^{2,3} Simon Schweidler,² Andreas Beyer,¹ Torsten Brezesinski,² Jürgen Janek,^{2,4*} and Kerstin Volz^{1*}

¹ Materials Science Center (WZMW) and Department of Physics, Philipps-University of Marburg, Marburg, Germany

² Battery and Electrochemistry Laboratory, Institute of Nanotechnology, Karlsruhe Institute of Technology (KIT), Hermann-von-Helmholtz-Platz 1, 76344 Eggenstein-Leopoldshafen, Germany

³ BASF SE, Carl-Bosch-Strasse 38, 67056 Ludwigshafen, Germany

⁴ Institute of Physical Chemistry & Center for Materials Research, Justus-Liebig-University, Heinrich-Buff-Ring 17, 35392 Giessen, Germany

Corresponding authors: Kerstin Volz (volz@staff.uni-marburg.de)

Jürgen Janek (Juergen.Janek@phys.Chemie.uni-giessen.de)

Summary

Layered $\text{Li}(\text{Ni}_{1-x-y}\text{Co}_x\text{Mn}_y)\text{O}_2$ (NCM, with $\text{Ni} \geq 0.8$) cathode materials are essential to achieve high energy densities in the next generation of lithium-ion batteries. This increased performance comes at the expense of stability. To extend the materials' lifetime, it is necessary to understand the role that crystal defects play in the degradation during electrochemical cycling. In this study, NCM851005 (85% Ni) is investigated in the pristine state and after 100 and 200 cycles using scanning transmission electron microscopy (STEM), with the focus being on the defects in the material. The formation of antiphase boundaries (APB) from a dislocation in a pristine sample is proven. After 100 cycles, the APBs' length and width are enlarged compared to the pristine state. After 200 cycles, APBs further evolve into an intragranular rock salt-like phase, distorting the nearby layered structure. It is suggested that the behavior of APBs plays a critical role in determining the performance of this cathode material with prolonged electrochemical cycling. These findings will help to understand better the role of dislocations and antiphase boundaries with electrochemical cycling, and the role of dopants may then be explored to avoid them.

Keywords

Batteries; cathode active material; dislocations, antiphase boundaries, twin boundaries, nanopores, layered phase, rock salt-like phase

Introduction

The successful commercialization of lithium-ion batteries (LIBs) has relied on layered oxide cathode active materials (CAMs), such as LiCoO_2 (LCO).¹ They have not only revolutionized the consumer electronics industry but also made electric vehicles possible. Especially for automotive applications, the original LCO cathode material has been replaced mainly by solid solution CAMs, $\text{Li}(\text{Ni}_{1-x-y}\text{Co}_x\text{Mn}_y)\text{O}_2$ (NCM)² and $\text{Li}(\text{Ni}_{1-x-y}\text{Co}_x\text{Al}_y)\text{O}_2$ (NCA),³ due to the high costs and environmental issues related to cobalt.^{4,5} Replacing cobalt completely with nickel and using LiNiO_2 (LNO) would be ideal for reducing the cost while simultaneously achieving a high energy density. However, significant difficulties lie in the stoichiometric synthesis of LNO (i.e. in controlling the Li/Ni ratio) and in its instability at high states of charge.⁶⁻¹⁰ Partially substituting nickel with cobalt, manganese, and aluminium has shown promising results and led to the successful development of CAMs like $\text{Li}(\text{Ni}_{0.33}\text{Co}_{0.33}\text{Mn}_{0.33})\text{O}_2$ (NCM111), $\text{Li}(\text{Ni}_{0.5}\text{Co}_{0.3}\text{Mn}_{0.2})\text{O}_2$ (NCM532), or $\text{Li}(\text{Ni}_{0.6}\text{Co}_{0.2}\text{Mn}_{0.2})\text{O}_2$ (NCM622).¹¹ Ni-rich NCM cathode materials (with $\geq 80\%$ Ni content) are intensively studied,¹² as higher specific capacities (for a given cut-off voltage) are expected compared to NCM containing less Ni.¹³⁻¹⁵ To date, structure-related limitations (e.g., phase transformations) plague their life cycle. These issues need to be better understood and mitigated to utilize their full potential.

Several degradation mechanisms have already been reported, including transition-metal (TM) dissolution,¹⁶⁻¹⁹ surface oxygen-loss and rock salt-like phase formation,²⁰⁻²³ secondary particle fracture,^{24,25} and intragranular cracking.²⁶⁻²⁸ Recently, the adverse effects of intragranular nanopores on the surrounding microstructure have been pointed out.²⁹ To suppress some of the degradation phenomena mentioned, various mitigation concepts are employed, such as coatings on primary³⁰ and secondary particles,^{31,32} doping,³³⁻³⁵ design of gradient and core-shell materials,^{36,37} and adding additives to the electrolyte.³⁸

The typical morphology of commercial CAMs comprises primary crystallites of about 100 nm in size, agglomerated into larger secondary particles of nearly spherical shape (5 - 20 μm diameter). The crystal structure of a typical primary particle is far from ideal. Several microstructural features like open surfaces,³⁹ coherent and incoherent grain boundaries,^{39,40} dislocations,⁴¹ stacking faults,⁴² intragranular nanopores,²⁹ and cracks²⁶ have been observed. These can be present in the pristine state or, more often, develop during electrochemical cycling (i.e., after repeated (de-)lithiation cycles). Their characterization is essential for understanding the behavior of primary particles upon battery operation. Usually, a primary particle is not a single crystal but rather is divided into subdomains separated by coherent grain boundaries (CGBs).⁴³ Two types of CGBs have been identified to date in NCM cathode materials in the literature, namely, twin boundaries (TBs)³⁹ and antiphase boundaries (APBs).⁴⁰ The presence of TBs and their role in favoring the rock salt-like phase formation has already been discussed in some detail.^{39,40} APBs are formed when the TM layers of a layered domain on one side are in contact with the Li layers of a layered domain on the other side.⁴⁰ Strictly speaking, these are not full antiphase boundaries as reported in the literature on alloys, but rather are cationic antiphase boundaries, i.e., they comprise two cations switching their positions, while the anionic sublattice is not affected.⁴⁴ Here, we will call them APBs for simplicity. Figure 1 shows schematic models of the APB and the TB, respectively. We note that APBs represent a

frequently occurring microstructural feature in layered NCM cathode materials, as they have been shown to exist in various layered CAMs but haven't been addressed explicitly yet.^{43,45,46} They especially occur in electrochemically cycled samples. Although their formation energies,⁴⁰ stability at higher temperatures⁴⁷ and ability to facilitate the Li transport have already been discussed,⁴⁸⁻⁵⁰ several crucial points – especially regarding battery operation - like their formation mechanism, evolution, and effect on the microstructure with prolonged cycling remain elusive. Hence, unlike these other studies, the present study has direct impact on the understanding of deterioration mechanisms during device operation.

In this study, we used aberration-corrected scanning transmission electron microscopy (AC-STEM)^{51,52} to explore the microstructure of primary particles in a large field-of-view, as well as at atomic resolution. We focus on dislocations and APBs leading to defect phase formation in $\text{Li}_{1-x}(\text{Ni}_{0.85}\text{Co}_{0.1}\text{Mn}_{0.05})_{1-x}\text{O}_2$ (NCM851005). Figure S1(a) shows the charge-discharge curves for the 100th and 200th cycles. An overview image of secondary particles and a typical TEM sample preparation procedure for secondary particles are shown in Figures S1(b-d). We firstly discuss dislocations and APBs in the pristine sample. Then, we show their evolution after the CAM has been cycled 100 times, followed by the effect of APBs in the formation of an intragranular rock salt-like phase in samples after 200 cycles. All results presented in this study are statistically relevant in a sense that all data shown is representative for several grains observed in different samples investigated. Our observations together with published studies,^{40,43,45-47} prove that APBs are an important defect, which is general to layered CAMs.

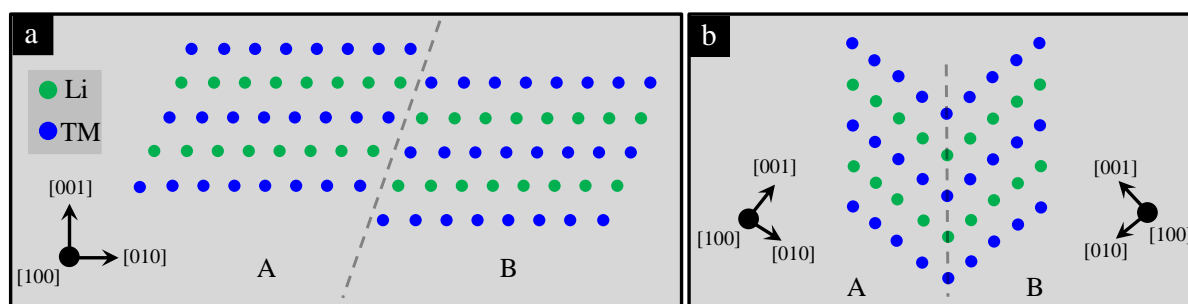


Figure 1: Simplified models of (a) an antiphase boundary and (b) a twin boundary. Lithium and transition metal (TM) atomic positions are shown by green and blue circles, respectively. Oxygen atomic positions are omitted. The dashed gray lines highlight boundaries in separating two crystal domains, ‘A’ on the left from ‘B’ on the right.

Results and discussion

Formation of APBs

Figure 2(a) shows a low-magnification high angle-annular dark-field (HAADF) image of a primary particle. Some intragranular nanopores are exemplarily marked with black arrows. Figure 2(b) is a high-resolution HAADF image of the region indicated by the black square in Figure 2(a). It shows the atomic-resolution image of a nanopore region. Figure 2(c) is the average background subtraction filtered (ABSF) image of Figure 2(b). Such filtering enhances

the contrast from the atomic positions.^{40,53,54} The area marked with the green-dashed lines denotes an APB. The region highlighted by the purple square in Figure 2(c) is shown in Figure 2(d) to elucidate the formation mechanism of the APB. The corresponding inverse fast Fourier transform (IFFT) images using the 003, 00-3 and 006, 00-6 reflections and the 0-11 and 01-1 reflections are shown in Figure 2(e) and Figure 2(f), respectively (see also FFT in Figure S2.1(a)). The yellow-dotted line in Figure 2(e) marks the extra (003) plane, indicating the presence of an edge dislocation. Dislocations are common in pristine layered cathode materials.⁴² Furthermore, Li et al.⁴⁰ calculated the energetic difference between the crystal structure of NCM76 with and without APB by Density Functional Theory as (only) 57 meV/atom, showing that APBs are not unlikely to exist in the pristine layered structure. The red-dotted circles in the upper half of Figure 2(f) highlight two extra-half (0-11) planes in opposite directions, a few nanometers apart from each other near the initiation point of the APB. Another pair of directionally opposite extra-half (0-11) planes can be seen in the bottom half of the image, further apart from each other, close to the position where the APB terminates. Figures S2.1(b,c) depict the ϵ_{xx} and ϵ_{yy} strain components extracted by geometric phase analysis (GPA) from Figure 2(d). The yellow and red arrows denote the same positions as in Figure 2(f). The marked points show dislocation cores. It is known that an APB in a layered compound is formed by partially translating the TM layer by a $1/6[211]$ lattice vector.⁴⁰ Since the $[211]$ lattice vector lies on the (0-11) plane (see also Figure S2.1(d)), tracking distortions of 0-11 and 01-1 reflections from the FFT makes the shift along these planes visible. The layered NCM cathode has an ordered crystal structure with alternating layers of TM- and Li along the $[001]$ direction. The extra-half (003) plane (in other words, an edge dislocation) disturbs the stacking sequence. Further movement of the dislocations through the lattice breaks up the layered ordering along the $[001]$ direction (i.e., across (003) slip planes). This causes the formation of pairs of coupled Shockley partial dislocations. Figures 3(a,b) show a model of an edge dislocation.²⁶ The movement of an edge dislocation through the crystal takes place by partially translating TM layers by $1/6[211]$, i.e. this is the Burgers vector of the Shockley partial dislocation. This movement of an edge dislocation together with partial translation of TM layers produces an APB, as shown in Figure 3(d) (see also the video in the Supplementary Information). In Figures 2(b-d) and 3(d), however, the edge dislocation has not been fully consumed by the APB, as the dislocation is still present and has not passed through the crystal completely. In an ordered material, when the dislocation is partially through the crystal and has not reached the surface of the crystal, APB and dislocation are present together (see also the video in the Supplementary Information).⁵⁵ Taken together, the results indicate that an edge dislocation's movement across the (003) plane can lead to the formation of APBs in this material. Since the dislocation and APB are present together in the pristine NCM851005 sample, we believe that the formation of the dislocation and its movement are likely to have occurred already during the synthesis process.

The present study is the first experimental observation of APB initiation from a dislocation in a pristine NCM cathode material. Li et al.⁴⁰ predicted that APBs could also form during electrochemical cycling at an early stage of delithiation at regions where lithium depletion is likely to occur. Such areas are dislocations, particle surfaces, and grain boundaries. Interestingly, we observed that the regions in and around nanopores usually contain a high

defect density, including dislocations, APBs, and lattice distortions. Hence, they might facilitate APB formation, as dislocations are shown to exist in the nanopore region, as indicated in Figure 2(b). Nevertheless, defects can also be found in the bulk structure of a primary particle (refer to Figures S2.2(a-d)).

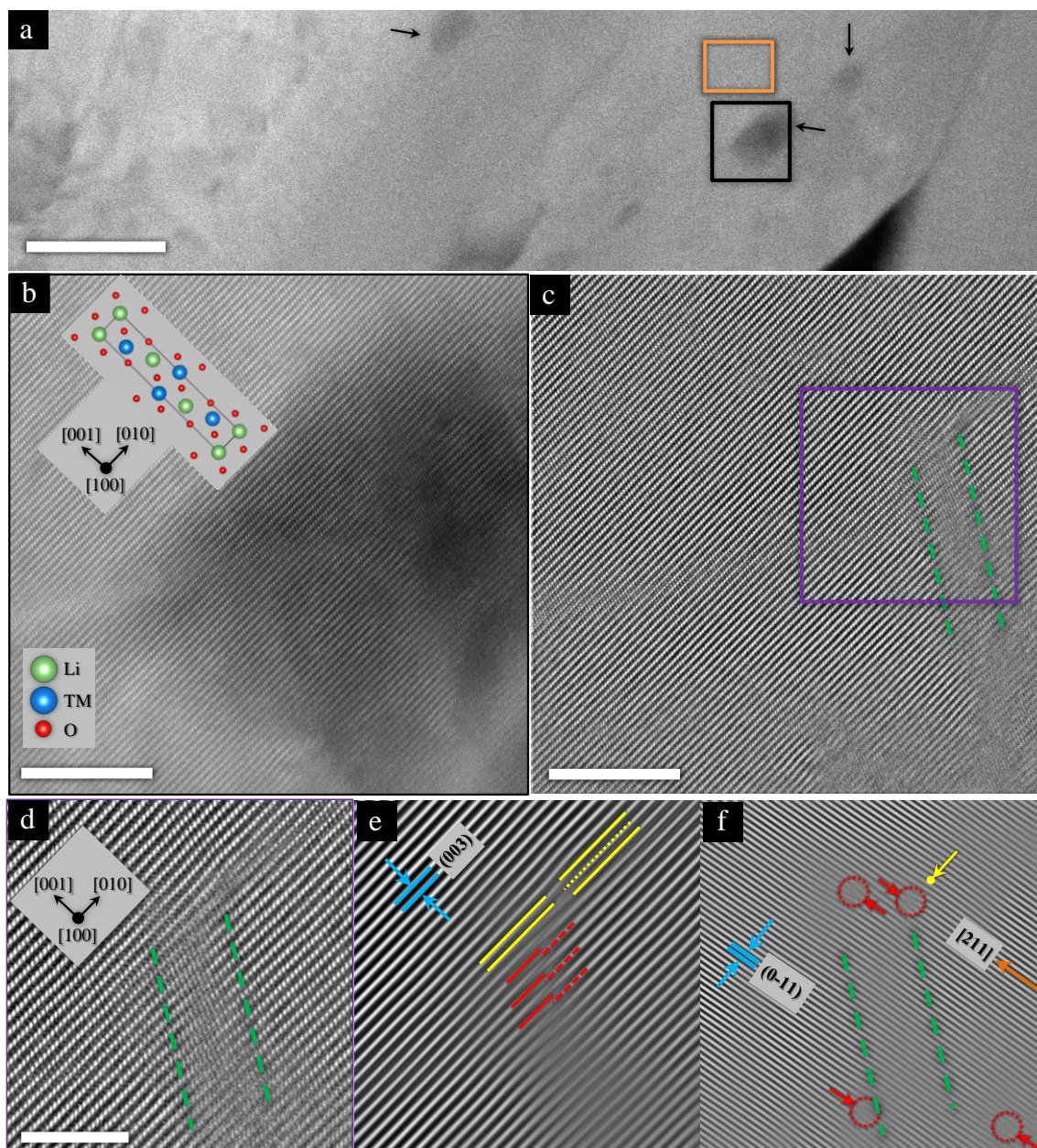


Figure 2: HAADF images of the pristine NCM851005 CAM. (a) Low-magnification image of a primary particle. (b) High-resolution image of the area marked with a black square in (a). (c) ABSF-filtered image of (b) with enhanced crystalline contrast. The dashed green lines enclose an APB. (d) Enlarged view of the region highlighted by the purple square in (c). Green-dashed lines mark the same regions as in (c). (e,f) IFFT images from 003/00-3 and 006/00-6 reflections, as well as 0-11 and 01-1 reflections (see also Figure S2.1(a)). The blue lines show (003) and (0-11) planes, respectively. The solid yellow lines show (003) planes at the edge dislocation in (e). The dotted yellow line shows an extra-half (003) plane. The solid and dashed red lines are used for eye guidance only, indicating two contacting (003) planes from two crystal domains at the APB. The red arrows and dotted red circles show extra-half (0-11) planes in (f). The yellow arrow (with the dot) points towards the position of the core of the edge dislocation along the (003) plane. The brown arrow highlights the [211] lattice direction in [100] projection (see also Figure S2.1(d)). Scale bars are 100 nm, 10 nm, and 5 nm in (a), (b,c), and (d), respectively.

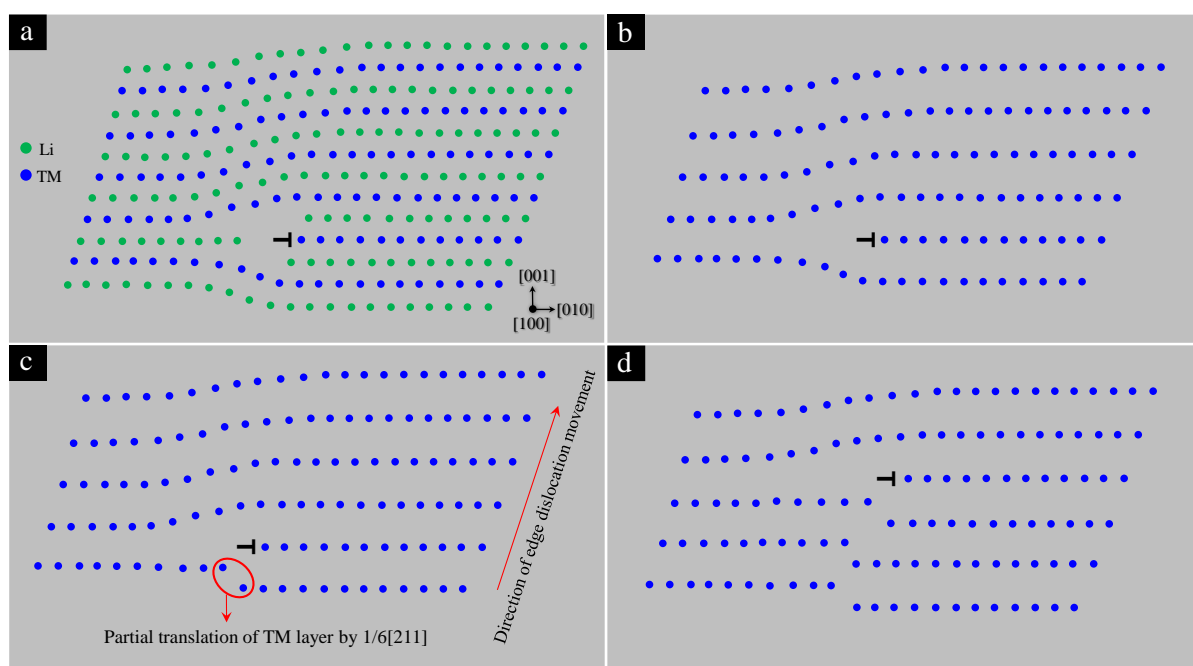


Figure 3: (a) A model of dislocation in NCM CAM adapted from ref.²⁶ Oxygen ions are omitted for clarity. (b) The same model as shown in (a) but without lithium ions. Note that both oxygen and lithium ions are omitted to make the model comparable to the HAADF images shown in Figures 2(b-d). (c) The potential first step when an edge dislocation moves through the crystal across the layered (003) planes. The movement is accompanied by a partial translation of TM layers by $1/6[211]$ lattice vector. (d) APB formation as the edge dislocation moves further through the crystal. The APB and dislocation are present together because the dislocation is not consumed completely (see also the video in the Supplementary Information).

Evolution of APBs during electrochemical cycling

APBs have been shown to extend with electrochemical cycling.⁴⁰ However, their effect on the microstructure of a primary particle with prolonged cycling is not clear. Figure 4(a) is a low-magnification HAADF image of primary particles after electrochemical cycling of the sample (100 cycles). It becomes increasingly challenging to bring the whole field-of-view of a primary particle simultaneously in the zone axis because of severe lattice distortions in the cycled material.⁵⁶ Figure 4(b) is a high-resolution HAADF image of the area highlighted by the red square in Figure 4(a). The green-dashed lines mark the APB passing through the nanopores' facet-intersection across the layered planes. The terms "length" and "width" (used hereafter) define the size of the APB across and along (003) planes, respectively, as shown in Figure 4(b). In contrast to the pristine material, in which the APB extends to only a few TM layers across the (003) planes, here the APBs have increased in length considerably. The length increment is attributed to further movement of partial dislocations with the Burgers vector $1/6[211]$.⁴⁰ Figure 4(b) demonstrates that the width of the APB has also enlarged significantly as compared to the one shown for the pristine sample (referred to as "broadened APB" hereafter). At the

APB, TM layers (along the (003) planes) from the left domain penetrate deeper laterally into the Li ion layers of the domain on the right (and vice versa). This is likely to happen during cycling in particular, because Li is extracted from the Li layers leaving vacant sites where Ni can easily diffuse. The computational studies conducted by Lee et al.⁵⁷ for APBs in LCO led to the conclusion that the lithium ion vacancies segregate near APBs during delithiation. Even though no analogous results have yet been reported for Ni-rich layered oxide CAMs, to the best of our knowledge, the conclusions from Lee et al.⁵⁷ can likely be extrapolated to Ni-rich NCMs due to their isostructural nature with LCO. One may then expect the nickel cations to migrate to the space left in the lithium layers at APBs, ultimately resulting in nickel segregation (rock salt-like formation) after prolonged lithium (de-)intercalation. It is important to note that the width of the APB is not constant but varies along its length. So, using the term width, we refer to the maximum width along the length of the APB. APBs' lengths and widths might vary depending on the surrounding microstructure, like the presence of free surfaces and grain boundaries and intragranular defects like nanopores, intragranular cracks, dislocations, TBs, and defective phases.

In the lower-left of **Figure 4(b)**, an FFT of the area highlighted by the blue square is shown, containing reflections forbidden in the rhombohedral symmetry. At first glance, they may appear to be related to a spinel-like structure. The blue oval marks the extra order of reflections in the FFT compared to the layered phase (see Figure S2.1(a)). The two FFTs in Figure S3.1(a) also show similar structures. Interestingly, however, these FFTs seem to match qualitatively the diffraction patterns of nickel-excess phases of the type $\text{Ni}_{0.25}\text{NiO}_2$ (referred to as β -phase) and $\text{Ni}_{0.5}\text{NiO}_2$ (referred to as γ -phase), as suggested by Xiao et al. and recently proven experimentally.^{58,59} The authors showed that these Ni-rich phases, in which Ni replaces Li, exist next to the surface-densified NiO-like (rock salt) phase in samples of LiNiO_2 and $\text{LiNi}_{0.8}\text{Al}_{0.2}\text{O}_2$ that underwent a single cycle. Here, we corroborate their findings by proving that the same phases in NCM samples cycled many times under realistic conditions (also shown later in the paper). Since the diffraction patterns of the β - and γ - Ni_xNiO_2 phases are similar, it is difficult to discern between these two phases completely with FFTs only.^{58,59} Because β and γ are transition phases between layered and cubic nickel oxide phases, we suggest that their existence also indicates that a broad APB behaves analogously to a rock salt-like region because of the considerable fraction of TM ions entering the Li layers.

Figure S3.2 shows the low-pass filtered image of Figure 4(b). The significant increase in mass thickness contrast observed in Figure 4(b) and Figure S3.2 further reveals the segregation of TM ions and the onset of rock salt phase formation. Like nanopores or open interfaces near APBs, free space might facilitate its broadening by allowing oxygen release. The broadening of an APB adversely affects the diffusion of lithium ions along the (003) planes, decreases the local lithium diffusion coefficient, and increases the cathode impedance.

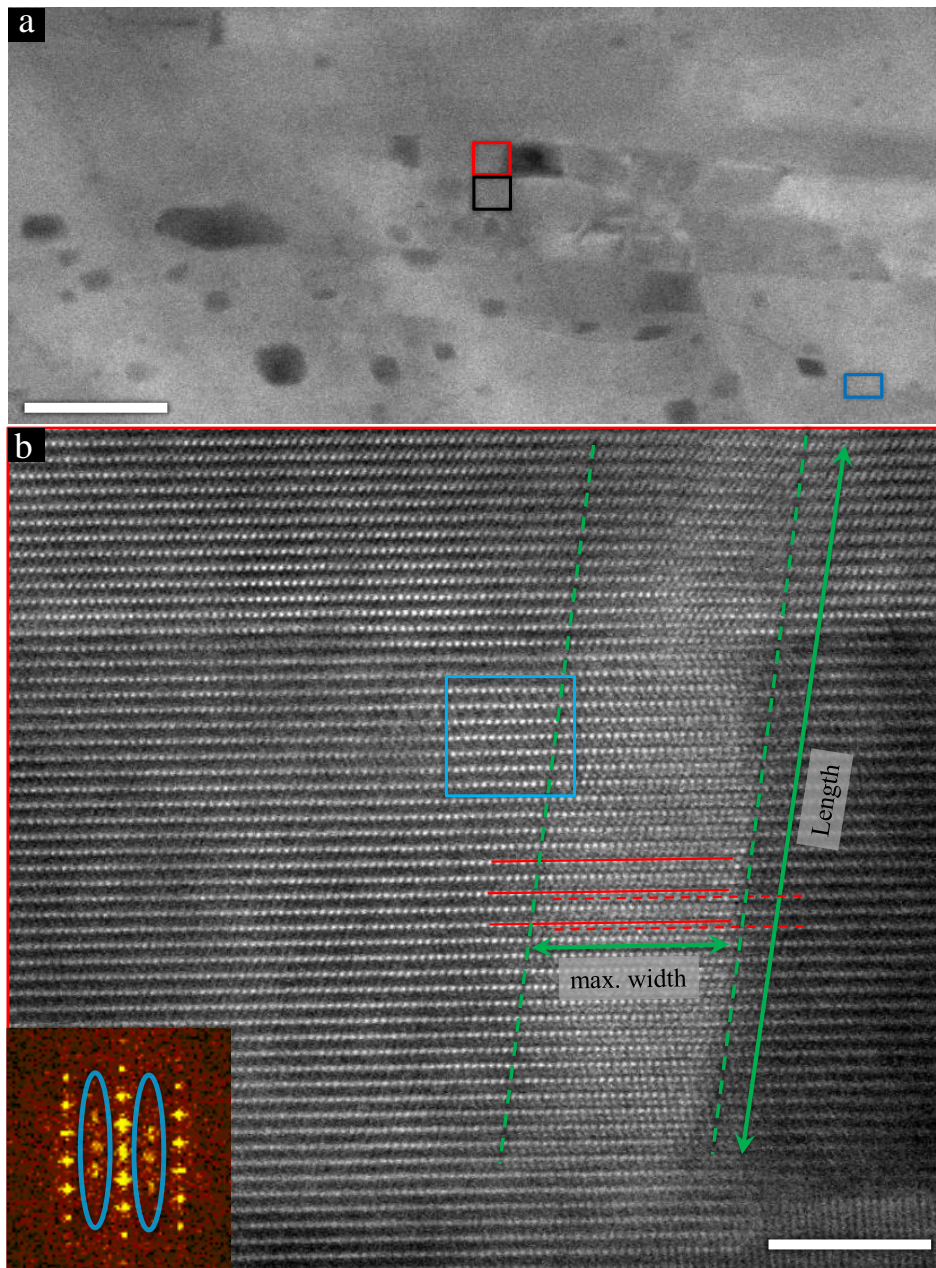


Figure 4: HAADF images of the NCM851005 CAM after 100 cycles. (a) Low-magnification image of a primary particle. The regions highlighted by the blue rectangle and black square are shown in Figures S3.1(a,b). (b) High-resolution HAADF image of the region highlighted by the red square in (a). The dashed green lines enclose a broadened APB. The solid and dashed red lines are used for eye guidance only, marking two interpenetrating TM layers. The length and maximum width of the APB are indicated by green double-headed arrows. On the lower left, an FFT of the area indicated by the blue square is shown. The blue ovals in the FFT denote a faint extra order of reflections compared to the FFT of the layered phase shown in Figure S2.1(a). Scale bars are 100 nm and 5 nm in (a) and (b), respectively.

NCM851005 CAM that underwent 200 cycles has also been investigated to further understand the evolution of APBs. Figure 5(a) shows a low-magnification HAADF image of a primary

particle. Figure 5(b) shows the atomic-resolution HAADF image of the region highlighted by the red square in Figure 5(a). The areas marked with dashed blue and green lines denote nanopores and APBs, respectively. The width of the APBs has further increased as compared to the sample cycled 100 times. The dashed yellow lines indicate the areas of low mass-thickness contrast and distorted layered structure around the APBs (see also Figure S4(a)).

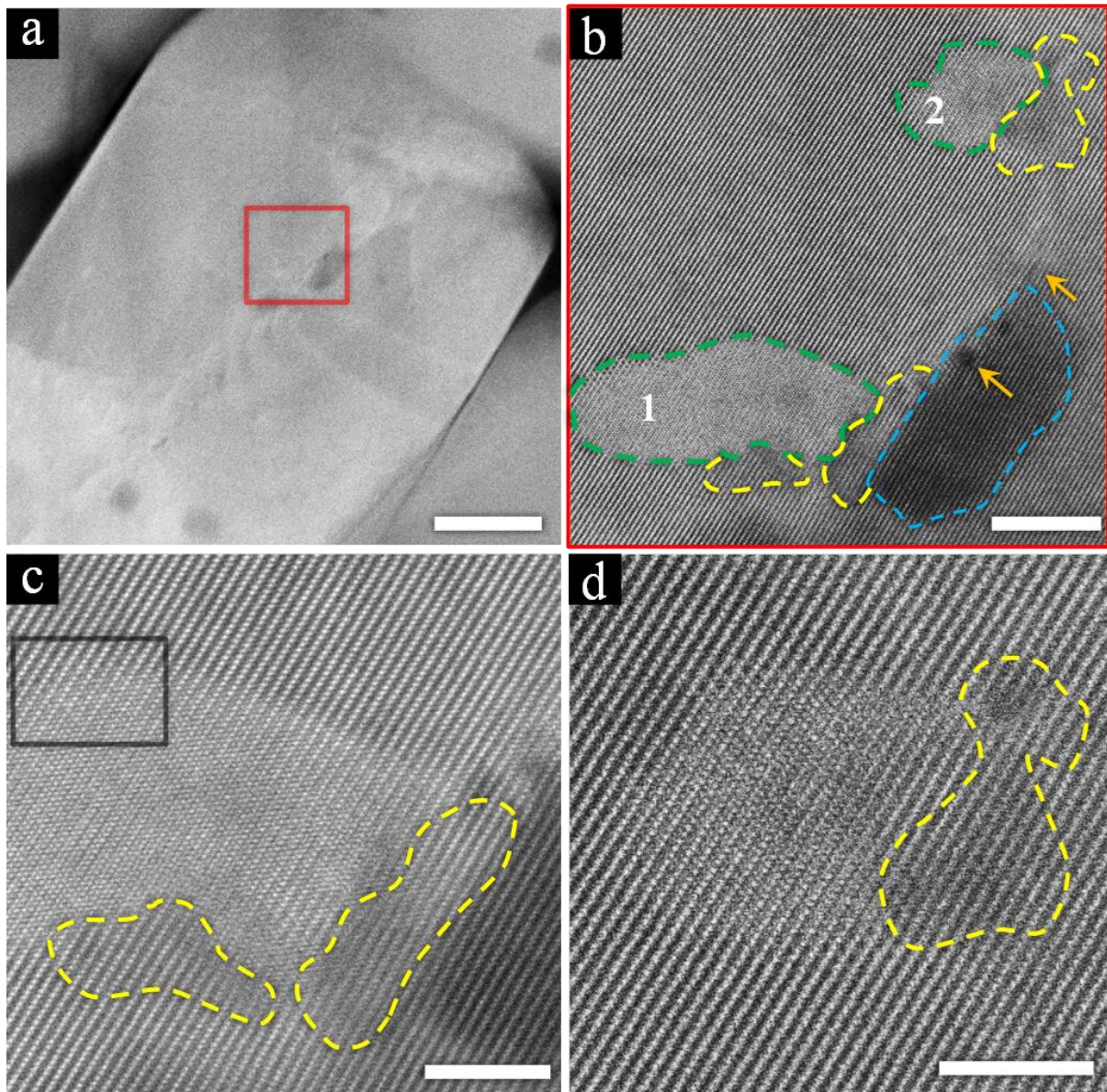


Figure 5: HAADF images of the NCM851005 CAM after 200 cycles. (a) Low-magnification image of a primary particle. (b) Atomic-resolution image of the region highlighted by the red square in (a). Dashed blue, green, and yellow lines enclose nanopores, broadened APBs, and low-mass thickness areas, respectively. Orange arrows mark edge dislocations along (003) planes. (c) Zoomed-in view of a region around the broadened APB 1 in (b). The area highlighted by the black square is shown in Figure S4(b). (d) Zoomed-in view of the region around APB 2 in (b). Dashed yellow curves mark low-mass thickness areas in (c,d). Scale bars are 50 nm, 10 nm, and 5 nm in (a), (b), and (c,d), respectively.

The orange arrows indicate edge dislocations along (003) planes. Figure 5(c) is a high-magnification (atomic-resolution) image of the region around the broadened APB 1. The APB seems significantly denser as compared to the one shown in Figure 4(b). The area marked with a black square again shows the β/γ phases (see Figure S4(b,c)). Figure 4(d) shows another broadened APB marked 2 in Figure 5(b). APBs 1 and 2 resemble a rock salt-like structure. The widening of APBs leads to a significant substitution of positions in the Li ion layers by TM ions. The larger width of APBs in the sample after 200 cycles and the associated β - and/or γ -phase fronts suggest that the local TM substitution is accompanied by oxygen release to satisfy the thermodynamic requirement for the formation of reduced nickel oxide phases at the core of the broadened APB. The low mass-thickness contrast areas denoted by dashed yellow curves around the APBs suggest that the TM ions have moved further towards the broadened APB core. In contrast to the broadened APB 1, there is no nanopore present in the vicinity of the broadened APB 2. This could explain why APB 2 has not evolved as much as APB 1 since there is less room for oxygen release in the nearby regions, thereby corroborating the role of nanopores as oxygen sinks and “facilitators” of structural degradation.

Figures 6(a-c) present a one-to-one (qualitative) comparison of APB evolution from pristine material (Figure 2(d)) to samples that were electrochemically cycled for 100 (Figure 4(b)) and 200 times (Figure 5(c)). We cannot specify at which stage of cycling the specific APBs in Figures 6(b,c) formed, but qualitatively a general trend can be deduced from these data. To gain further insight, we traced TM layers from two connected crystalline domains with lines shown partially in the atomic-resolution images in Figures 6(a-c) and separately in Figures 6(d-f). **TM layers from the left- and right-hand sides are traced with solid and dashed red lines, respectively.** Compared to Figure 6(a), the TM layers from one layered domain penetrate deeper into the Li layer of the other layered domain in Figure 6(b) (and vice versa). The interpenetrating TM layers form pairs, with each pair having TM layers from two different domains slightly closer to each other. The distance between the TM layers of these pairs is larger than the distance between interpenetrating TM layers in each pair (see also Figure S5). While interpenetrating TM layers from two different domains can be distinguished in Figure 6(b), this is different in Figure 6(c) and holds up to only a few TM layers present at the bottom (indicated by the blue arrow). At the bottom of Figures 6(c,f), TM layers from the domain on the right follow a straight path along the (003) planes. However, the domain on the left shows discontinuous TM layers with considerable plane bending. Interestingly, from the position indicated by the blue arrow in Figures 6(c,f), **the solid yellow lines show bright intensities from the atomic positions of lithium ions.** From this position, the TM layers from the left layered domain, through the APB towards the layered domain on the right, are along the same planes, unlike typical interpenetrating TM layers at the broad APB in Figure 6(b). In addition, there are also TM ions visible in the Li layers. This indicates that the broadened APB has evolved into an intragranular rock salt-like structure that is coherently intergrown with the layered structure. The background intensity in Figure 6(c) has changed significantly compared to Figure 6(b), also suggesting that a rock salt-like phase has formed (see also low-pass filtered image in Figure S4(a)).

In summary, we have found APBs to originate from edge dislocations (present in the pristine CAM). It is known that electrochemical cycling can induce additional dislocations in the microstructure.^{26,27,60} To prove that APBs form in layered CAMs during charging, we investigated material charged to a voltage corresponding to the H2/H3 phase transition. For this study we choose LNO secondary particles as the higher the Ni-content the more severe the influence of electrochemical cycling (for micrographs of pristine LNO please see Figure S6.1). The secondary particles were extracted from the cell and were analyzed using high-resolution AC-STEM, as shown in Figure S6.2. The structure at the H2/H3 phase transition appears as a wavy-layered structure with a high density of short-length APBs, underlining the generality of our findings. We speculate that the formation of new APBs from the electrochemically-induced dislocations and their respective growth in length and width can be thought of as a recurring process with the increasing number of cycles. Interestingly, Gong et al.⁶¹ observed the formation of APBs in their *in-situ* TEM studies on spinel-type $\text{LiNi}_{0.5}\text{Mn}_{1.5}\text{O}_4$ (LNMO) during cycling. They found APBs to be detrimental to the structural integrity of the material. They also predicted from their calculations that doping spinel-type LNMO with low valance cations like Mg^{2+} might help suppress APB formation in LNMO.

Ultimately, as proven in our present study, APBs in Ni-rich NCM can transform locally into an intragranular rock salt-like phase. We also expect that faster charging rates will further promote APB formation. This dynamic behavior makes them particularly interesting and relevant for actual electrochemically-induced transformations. While so far it was unclear how APB's growth and widening would affect the CAM performance, here we have shown for the first time the potentially severe effect of APBs on the surrounding structure during cycling. Other studies, such as the one of Pokle et al.,⁴⁷ found APBs in NCM to be stable but dynamic at elevated temperatures, suggesting that compositional variations (i.e., delithiation) may be the leading factors driving APBs' evolution.

Conclusions

The formation and evolution of intragranular structural defects in Ni-rich NCM CAMs are complex phenomena that require careful investigation. We observed that APBs are present in pristine and electrochemically cycled NCM851005, and we showed their formation from dislocations in a pristine sample. Over cycling 100 times, APBs grow and widen, creating a double stripe-like appearance in high-resolution images. Moreover, APB regions were found to be bordered by narrow rock salt-like regions whose IFFT indicates the presence of the elusive $\text{Ni}_{0.25}\text{NiO}_2$ (β) and $\text{Ni}_{0.5}\text{NiO}_2$ (γ) phases suggested by Xiao et al.⁵⁸ This broadening certainly lowers the lithium diffusivity along the layered planes, as their path can be blocked by intergrowing Ni layers. After 200 cycles, APBs evolve into an intragranular rock salt-like structure (mostly) coherently intergrown with the surrounding layered phase. The formation of the rock salt-like phase is accompanied by oxygen release in the surrounding phase. Overall, APBs increase the fraction of the electrochemically inactive rock salt-like phase in the primary particle and distort the surrounding structure. Hence, they have an adverse effect on the longevity of the CAM. We propose that the role of dopants should be explored to suppress the formation of APBs, as has been done for LNMO by Gong et al.⁶¹ Similarly, a theoretical study might also be conducted to explore possible dopants for Ni-rich layered CAMs (starting from

Mg for example) to suppress APB formation. Furthermore, a co-doping strategy can also be explored in this regard.⁶²

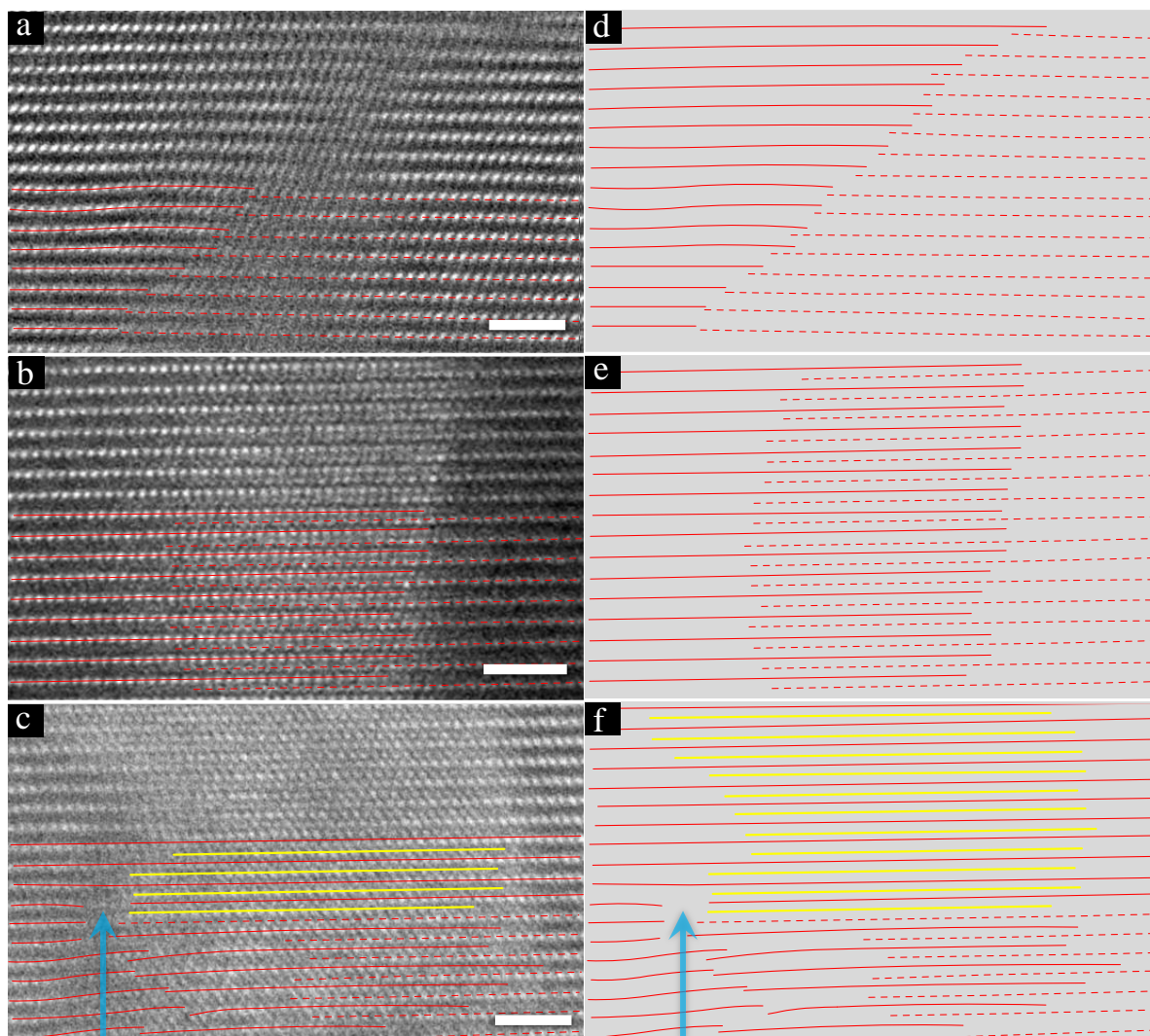


Figure 6: (a-c) High-resolution HAADF images of APB cores from the pristine NCM851005 CAM (Figure 2(d)) and from samples after 100 (Figure 4(b)) and 200 (Figure 5(c)) cycles. (d-f) The corresponding line traces for the TM layers from the left- and right-hand sides of the APBs in (a-c) marked with solid and dashed red lines, respectively. The solid yellow lines in (c,f) show TM ions in the Li layers. Blue arrows denote the TM layers, after which the rock salt-like phase starts to become coherent with the layered phase. After this position, TM ions are also present in the TM-layer. Scale bars are 5 nm.

Experimental procedures

Resource availability

Lead contact

Further information and requests for resources should be directed to and will be fulfilled by the lead contact, Shamail Ahmed (shamail.ahmed@physik.uni-marburg.de).

Materials availability

This study did not generate new reagents.

Data and code availability

The authors declare that the data supporting the findings are available within the article and the supporting information. All other data are available from the lead contact upon reasonable request.

Cathode active material and electrochemical cycling

Industrial grade NCM851005 CAM with a chemical formula of $\text{Li}_{1+x}(\text{Ni}_{0.85}\text{Co}_{0.1}\text{Mn}_{0.05})_{1-x}\text{O}_2$ was selected for this study. It was tested in full (pouch) cells against a graphite anode with LP472 electrolyte and Celgard 2500 polypropylene separator. The cells were cycled in the voltage range of 2.8-4.2 V at a rate of 1C. The synthesis method, chemical composition of the electrolyte, and cycling procedures applied are detailed elsewhere.^{63,64}

TEM sample preparation

The electrodes were sputter-coated with platinum using a Leica EM ACE600 and then transferred to a focused-ion beam/scanning electron microscope (FIB/SEM). A JEOL JIB-4601F FIB-SEM was used for sample preparation. The samples were prepared from pristine NCM851005 and material after 100 and 200 cycles. As an example, Figure S1(b) shows the secondary particles in a cathode after 100 cycles. A secondary particle was coated with carbon and tungsten and then attached to a micromanipulator needle, as shown in Figure S1(c). The sample was attached to the TEM grid and thinned down further (see Figure S1(d)). Initial thinning was done using a 30 kV Ga-ion beam to roughly about 200 nm thickness. The sample was further thinned down to less than 100 nm using a 5 kV Ga-ion beam. Final thinning was performed using Ar-ion beams of 900 eV using Fischione NanoMill 1040 to reduce amorphous layers.

Electron microscopy

Low-magnification and atomic-resolution HAADF imaging were done using a double Cs-corrected JEOL JEM-2200FS transmission electron microscope (TEM) in STEM mode. The operating voltage and convergence angles were 200 kV and 15.07 mrad, respectively. An electron beam current of less than 10 pA was used. The inner and outer angles of the annular dark-field (ADF) detector were set to 70 and 280 mrad, respectively. All atomic-resolution images are shown in $\langle 100 \rangle$ zone axis.

ABSF⁵³ filter is applied by using the HRTEM Filter script available for DigitalMicrographTM.⁶⁵ GPA analysis⁶⁶ is done by using the FRWRTools plugin available free for DigitalMicrographTM.⁶⁷

Acknowledgment

Funding from Bundesministerium für Bildung und Forschung (BMBF) within the FESTBATT cluster of competence (project 03XP0176C) is gratefully acknowledged. This work was also supported by BASF SE.

Author Contributions

Conceptualization, S.A.; methodology, S.A. and A.P.; validation, S.A. and K.V.; formal analysis, S.A.; investigation, S.A.; resources, K.V., A.B., S.S., M.B., J.J., and T.B.; writing – original draft, S.A., M.B., and T.B.; writing – review & editing, S.A., K.V., A.P., M.B., and T.B.; supervision, K.V., A.B., M.B., J.J., and T.B.; project administration, A.B., K.V., J.J. and M.B.; funding acquisition, K.V. and J.J.

Author information

Anuj Pokle: <https://orcid.org/0000-0002-7457-8839>

Matteo Bianchini: <https://orcid.org/0000-0003-4034-7706>

Torsten Brezesinski: <https://orcid.org/0000-0002-4336-263X>

Jürgen Janek: <https://orcid.org/0000-0002-9221-4756>

Declaration of Interests

The authors declare no competing interests.

Supplementary material

Supplementary Information is available.

References

(1) Lyu, Y.; Wu, X.; Wang, K.; Feng, Z.; Cheng, T.; Liu, Y.; Wang, M.; Chen, R.; Xu, L.; Zhou, J.; Lu, Y.; Guo, B. An Overview on the Advances of LiCoO₂ Cathodes for Lithium-Ion Batteries. *Adv. Energy Mater.* **2021**, *11* (2), 2000982. <https://doi.org/10.1002/aenm.202000982>.

- (2) Xu, J.; Lin, F.; M. Doeff, M.; Tong, W. A Review of Ni-Based Layered Oxides for Rechargeable Li-Ion Batteries. *J. Mater. Chem. A* **2017**, *5* (3), 874–901. <https://doi.org/10.1039/C6TA07991A>.
- (3) Li, W.; Erickson, E. M.; Manthiram, A. High-Nickel Layered Oxide Cathodes for Lithium-Based Automotive Batteries. *Nat. Energy* **2020**, *5* (1), 26–34. <https://doi.org/10.1038/s41560-019-0513-0>.
- (4) Ryu, H.-H.; Hohyun Sun, H.; Myung, S.-T.; S. Yoon, C.; Sun, Y.-K. Reducing Cobalt from Lithium-Ion Batteries for the Electric Vehicle Era. *Energy Environ. Sci.* **2021**, *14* (2), 844–852. <https://doi.org/10.1039/D0EE03581E>.
- (5) Harlow, J. E.; Ma, X.; Li, J.; Logan, E.; Liu, Y.; Zhang, N.; Ma, L.; Glazier, S. L.; Cormier, M. M. E.; Genovese, M.; Buteau, S.; Cameron, A.; Stark, J. E.; Dahn, J. R. A Wide Range of Testing Results on an Excellent Lithium-Ion Cell Chemistry to Be Used as Benchmarks for New Battery Technologies. *J. Electrochem. Soc.* **2019**, *166* (13), A3031. <https://doi.org/10.1149/2.0981913jes>.
- (6) Bianchini, M.; Roca-Ayats, M.; Hartmann, P.; Brezesinski, T.; Janek, J. There and Back Again - The Journey of LiNiO₂ as Cathode Active Material. *Angew. Chem. Int. Ed.* **58**, 10434–10458. <https://doi.org/10.1002/anie.201812472>.
- (7) Bianchini, M.; Fauth, F.; Hartmann, P.; Brezesinski, T.; Janek, J. An in Situ Structural Study on the Synthesis and Decomposition of LiNiO₂. *J. Mater. Chem. A* **2019**, 1808–1820. <https://doi.org/10.1039/C9TA12073D>.
- (8) Ahmed, S.; Bianchini, M.; Pokle, A.; Munde, M. S.; Hartmann, P.; Brezesinski, T.; Beyer, A.; Janek, J.; Volz, K. Visualization of Light Elements Using 4D STEM: The Layered-to-Rock Salt Phase Transition in LiNiO₂ Cathode Material. *Adv. Energy Mater.* **2020**, *10* (25), 2001026. <https://doi.org/10.1002/aenm.202001026>.
- (9) Li, H.; Zhang, N.; Li, J.; Dahn, J. R. Updating the Structure and Electrochemistry of Li_xNiO₂ for 0 ≤ x ≤ 1. *J. Electrochem. Soc.* **2018**, *165* (13), A2985–A2993. <https://doi.org/10.1149/2.0381813jes>.
- (10) Delmas, C.; Croguennec, L. Layered Li(Ni,M)O₂ Systems as the Cathode Material in Lithium-Ion Batteries. *MRS Bull.* **2002**, *27* (8), 608–612. <https://doi.org/10.1557/mrs2002.196>.
- (11) Schipper, F.; Nayak, P. K.; Erickson, E. M.; Amalraj, S. F.; Srur-Lavi, O.; Penki, T. R.; Talianker, M.; Grinblat, J.; Sclar, H.; Breuer, O.; Julien, C. M.; Munichandraiah, N.; Kovacheva, D.; Dixit, M.; Major, D. T.; Markovsky, B.; Aurbach, D. Study of Cathode Materials for Lithium-Ion Batteries: Recent Progress and New Challenges. *Inorganics* **2017**, *5* (2), 32. <https://doi.org/10.3390/inorganics5020032>.
- (12) Schmuch, R.; Wagner, R.; Hörpel, G.; Placke, T.; Winter, M. Performance and Cost of Materials for Lithium-Based Rechargeable Automotive Batteries. *Nat. Energy* **2018**, *3* (4), 267–278. <https://doi.org/10.1038/s41560-018-0107-2>.

- (13) Schipper, F.; Erickson, E. M.; Erk, C.; Shin, J.-Y.; Chesneau, F. F.; Aurbach, D. Review—Recent Advances and Remaining Challenges for Lithium Ion Battery Cathodes I. Nickel-Rich, $\text{LiNi}_x\text{Co}_y\text{Mn}_z\text{O}_2$. *J. Electrochem. Soc.* **2017**, *164* (1), A6220–A6228. <https://doi.org/10.1149/2.0351701jes>.
- (14) Li, W.; Liu, X.; Celio, H.; Smith, P.; Dolocan, A.; Chi, M.; Manthiram, A. Mn versus Al in Layered Oxide Cathodes in Lithium-Ion Batteries: A Comprehensive Evaluation on Long-Term Cyclability. *Adv. Energy Mater.* **2018**, *8* (15), 1703154. <https://doi.org/10.1002/aenm.201703154>.
- (15) Manthiram, A.; Song, B.; Li, W. A Perspective on Nickel-Rich Layered Oxide Cathodes for Lithium-Ion Batteries. *Energy Storage Mater.* **2017**, *6*, 125–139. <https://doi.org/10.1016/j.ensm.2016.10.007>.
- (16) Wandt, J.; Freiberg, A.; Thomas, R.; Gorlin, Y.; Siebel, A.; Jung, R.; Gasteiger, H. A.; Tromp, M. Transition Metal Dissolution and Deposition in Li-Ion Batteries Investigated by Operando X-Ray Absorption Spectroscopy. *J. Mater. Chem. A* **2016**, *4* (47), 18300–18305. <https://doi.org/10.1039/C6TA08865A>.
- (17) Hawley, W. B.; Parejiya, A.; Bai, Y.; Meyer, H. M.; Wood, D. L.; Li, J. Lithium and Transition Metal Dissolution Due to Aqueous Processing in Lithium-Ion Battery Cathode Active Materials. *J. Power Sources* **2020**, *466*, 228315. <https://doi.org/10.1016/j.jpowsour.2020.228315>.
- (18) Sahore, R.; O’Hanlon, D. C.; Tornheim, A.; Lee, C.-W.; Garcia, J. C.; Iddir, H.; Balasubramanian, M.; Bloom, I. Revisiting the Mechanism Behind Transition-Metal Dissolution from Delithiated $\text{LiNi}_x\text{Mn}_y\text{Co}_z\text{O}_2$ (NMC) Cathodes. *J. Electrochem. Soc.* **2020**, *167* (2), 020513. <https://doi.org/10.1149/1945-7111/ab6826>.
- (19) Asl, H. Y.; Manthiram, A. Reining in Dissolved Transition-Metal Ions. *Science* **2020**, *369* (6500), 140–141. <https://doi.org/10.1126/science.abc5454>.
- (20) Karki, K.; Huang, Y.; Hwang, S.; Gamalski, A. D.; Whittingham, M. S.; Zhou, G.; Stach, E. A. Tuning the Activity of Oxygen in $\text{LiNi}_{0.8}\text{Co}_{0.15}\text{Al}_{0.05}\text{O}_2$ Battery Electrodes. *ACS Appl. Mater. Interfaces* **2016**, *8* (41), 27762–27771. <https://doi.org/10.1021/acsami.6b09585>.
- (21) Boulineau, A.; Simonin, L.; Colin, J.-F.; Bourbon, C.; Patoux, S. First Evidence of Manganese–Nickel Segregation and Densification upon Cycling in Li-Rich Layered Oxides for Lithium Batteries. *Nano Lett.* **2013**, *13* (8), 3857–3863. <https://doi.org/10.1021/nl4019275>.
- (22) Zhang, H.; Omenya, F.; Yan, P.; Luo, L.; Whittingham, M. S.; Wang, C.; Zhou, G. Rock-Salt Growth-Induced (003) Cracking in a Layered Positive Electrode for Li-Ion Batteries. *ACS Energy Lett.* **2017**, *2* (11), 2607–2615. <https://doi.org/10.1021/acsenergylett.7b00907>.
- (23) Zheng, J.; Yan, P.; Zhang, J.; Engelhard, M. H.; Zhu, Z.; Polzin, B. J.; Trask, S.; Xiao, J.; Wang, C.; Zhang, J. Suppressed Oxygen Extraction and Degradation of $\text{LiNi}_x\text{Mn}_y\text{Co}_z\text{O}_2$

Cathodes at High Charge Cut-off Voltages. *Nano Res.* **2017**, *10* (12), 4221–4231. <https://doi.org/10.1007/s12274-017-1761-6>.

(24) Kondrakov, A. O.; Schmidt, A.; Xu, J.; Geßwein, H.; Mönig, R.; Hartmann, P.; Sommer, H.; Brezesinski, T.; Janek, J. Anisotropic Lattice Strain and Mechanical Degradation of High- and Low-Nickel NCM Cathode Materials for Li-Ion Batteries. *J. Phys. Chem. C* **2017**, *121* (6), 3286–3294. <https://doi.org/10.1021/acs.jpcc.6b12885>.

(25) Yoon, C. S.; Jun, D.-W.; Myung, S.-T.; Sun, Y.-K. Structural Stability of LiNiO₂ Cycled above 4.2 V. *ACS Energy Lett.* **2017**, *2* (5), 1150–1155. <https://doi.org/10.1021/acseenergylett.7b00304>.

(26) Yan, P.; Zheng, J.; Gu, M.; Xiao, J.; Zhang, J.-G.; Wang, C.-M. Intragranular Cracking as a Critical Barrier for High-Voltage Usage of Layer-Structured Cathode for Lithium-Ion Batteries. *Nat. Commun.* **2017**, *8*, 14101.

(27) Yan, P.; Zheng, J.; Chen, T.; Luo, L.; Jiang, Y.; Wang, K.; Sui, M.; Zhang, J.-G.; Zhang, S.; Wang, C. Coupling of Electrochemically Triggered Thermal and Mechanical Effects to Aggravate Failure in a Layered Cathode. *Nat. Commun.* **2018**, *9* (1), 2437. <https://doi.org/10.1038/s41467-018-04862-w>.

(28) Min, K.; Cho, E. Intrinsic Origin of Intra-Granular Cracking in Ni-Rich Layered Oxide Cathode Materials. *Phys. Chem. Chem. Phys.* **2018**, *20* (14), 9045–9052. <https://doi.org/10.1039/C7CP06615E>.

(29) Ahmed, S.; Pokle, A.; Schweidler, S.; Beyer, A.; Bianchini, M.; Walther, F.; Mazilkin, A.; Hartmann, P.; Brezesinski, T.; Janek, J.; Volz, K. The Role of Intragranular Nanopores in Capacity Fade of Nickel-Rich Layered Li(Ni_{1-x-y}Co_xMn_y)O₂ Cathode Materials. *ACS Nano* **2019**, *13* (9), 10694–10704. <https://doi.org/10.1021/acsnano.9b05047>.

(30) Xu, G.-L.; Liu, Q.; Lau, K. K. S.; Liu, Y.; Liu, X.; Gao, H.; Zhou, X.; Zhuang, M.; Ren, Y.; Li, J.; Shao, M.; Ouyang, M.; Pan, F.; Chen, Z.; Amine, K.; Chen, G. Building Ultraconformal Protective Layers on Both Secondary and Primary Particles of Layered Lithium Transition Metal Oxide Cathodes. *Nat. Energy* **2019**, *4* (6), 484–494. <https://doi.org/10.1038/s41560-019-0387-1>.

(31) Neudeck, S.; Mazilkin, A.; Reitz, C.; Hartmann, P.; Janek, J.; Brezesinski, T. Effect of Low-Temperature Al₂O₃ ALD Coating on Ni-Rich Layered Oxide Composite Cathode on the Long-Term Cycling Performance of Lithium-Ion Batteries. *Sci. Rep.* **2019**, *9* (1), 5328. <https://doi.org/10.1038/s41598-019-41767-0>.

(32) Weber, D.; Tripković, Đ.; Kretschmer, K.; Bianchini, M.; Brezesinski, T. Surface Modification Strategies for Improving the Cycling Performance of Ni-Rich Cathode Materials. *Eur. J. Inorg. Chem.* **2020**, *2020* (33), 3117–3130. <https://doi.org/10.1002/ejic.202000408>.

(33) Ryu, H.-H.; Park, G.-T.; Yoon, C. S.; Sun, Y.-K. Suppressing Detrimental Phase Transitions via Tungsten Doping of LiNiO₂ Cathode for Next-Generation Lithium-Ion

Batteries. *J. Mater. Chem. A* **2019**, *7* (31), 18580–18588. <https://doi.org/10.1039/C9TA06402H>.

(34) Kitsche, D.; Schweidler, S.; Mazilkin, A.; Geßwein, H.; Fauth, F.; Suard, E.; Hartmann, P.; Brezesinski, T.; Janek, J.; Bianchini, M. The Effect of Gallium Substitution on the Structure and Electrochemical Performance of LiNiO₂ in Lithium-Ion Batteries. *Mater. Adv.* **2020**, *1* (4), 639–647. <https://doi.org/10.1039/D0MA00163E>.

(35) Kim, H.; Jang, J.; Byun, D.; Kim, H.-S.; Choi, W. Selective TiO₂ Nanolayer Coating by Polydopamine Modification for Highly Stable Ni-Rich Layered Oxides. *ChemSusChem* **2019**, *12* (24), 5253–5264. <https://doi.org/10.1002/cssc.201902998>.

(36) Song, L.; Jiang, P.; Xiao, Z.; Cao, Z.; Zhou, C.; Du, J.; Liu, P. Core-Shell Structure LiNi_{0.8}Co_{0.1}Mn_{0.1}O₂ Cathode Material with Improved Electrochemical Performance at High Voltage. *Ionic*s **2021**, *27* (3), 949–959. <https://doi.org/10.1007/s11581-020-03893-y>.

(37) Hua, W.; Schwarz, B.; Azmi, R.; Müller, M.; Dewi Darma, M. S.; Knapp, M.; Senyshyn, A.; Heere, M.; Missyul, A.; Simonelli, L.; Binder, J. R.; Indris, S.; Ehrenberg, H. Lithium-Ion (de)Intercalation Mechanism in Core-Shell Layered Li(Ni,Co,Mn)O₂ Cathode Materials. *Nano Energy* **2020**, *78*, 105231. <https://doi.org/10.1016/j.nanoen.2020.105231>.

(38) Zhan, C.; Wu, T.; Lu, J.; Amine, K. Dissolution, Migration, and Deposition of Transition Metal Ions in Li-Ion Batteries Exemplified by Mn-Based Cathodes – a Critical Review. *Energy Environ. Sci.* **2018**, *11* (2), 243–257. <https://doi.org/10.1039/C7EE03122J>.

(39) Zou, L.; Zhao, W.; Jia, H.; Zheng, J.; Li, L.; Abraham, D. P.; Chen, G.; Croy, J. R.; Zhang, J.-G.; Wang, C. The Role of Secondary Particle Structures in Surface Phase Transitions of Ni-Rich Cathodes. *Chem. Mater.* **2020**, *32* (7), 2884–2892. <https://doi.org/10.1021/acs.chemmater.9b04938>.

(40) Li, S.; Yao, Z.; Zheng, J.; Fu, M.; Cen, J.; Hwang, S.; Jin, H.; Orlov, A.; Gu, L.; Wang, S.; Chen, Z.; Su, D. Direct Observation of Defect-Aided Structural Evolution in Ni-Rich Layered Cathode. *Angew. Chem. Int. Ed.* **2020**, *59* (49), 22092–22099. <https://doi.org/10.1002/anie.202008144>.

(41) Gabrisch, H.; Yazami, R.; Fultz, B. The Character of Dislocations in LiCoO₂. *Electrochem. Solid State Lett.* **2002**, *5* (6), A111. <https://doi.org/10.1149/1.1472257>.

(42) Xu, Z.; Hou, D.; Kautz, D. J.; Liu, W.; Xu, R.; Xiao, X.; Lin, F. Charging Reactions Promoted by Geometrically Necessary Dislocations in Battery Materials Revealed by In Situ Single-Particle Synchrotron Measurements. *Adv. Mater.* **2020**, *32* (37), 2003417. <https://doi.org/10.1002/adma.202003417>.

(43) Lee, S.-Y.; Park, G.-S.; Jung, C.; Ko, D.-S.; Park, S.-Y.; Kim, H. G.; Hong, S.-H.; Zhu, Y.; Kim, M. Revisiting Primary Particles in Layered Lithium Transition-Metal Oxides and Their Impact on Structural Degradation. *Adv. Sci.* **2019**, *6* (6), 1800843. <https://doi.org/10.1002/advs.201800843>.

- (44) Tabata, H.; Ishii, E.; Okuda, H. Cation Antiphase Boundaries in Ionic Crystals Based on Anion Close Packing. *J. Cryst. Growth* **1981**, *52*, 956–962. [https://doi.org/10.1016/0022-0248\(81\)90405-X](https://doi.org/10.1016/0022-0248(81)90405-X).
- (45) Gong, Y.; Zhang, J.; Jiang, L.; Shi, J.-A.; Zhang, Q.; Yang, Z.; Zou, D.; Wang, J.; Yu, X.; Xiao, R.; Hu, Y.-S.; Gu, L.; Li, H.; Chen, L. In Situ Atomic-Scale Observation of Electrochemical Delithiation Induced Structure Evolution of LiCoO₂ Cathode in a Working All-Solid-State Battery. *J. Am. Chem. Soc.* **2017**, *139* (12), 4274–4277. <https://doi.org/10.1021/jacs.6b13344>.
- (46) Chae, B.-G.; Park, S. Y.; Song, J. H.; Lee, E.; Jeon, W. S. Evolution and Expansion of Li Concentration Gradient during Charge–Discharge Cycling. *Nat. Commun.* **2021**, *12* (1), 3814. <https://doi.org/10.1038/s41467-021-24120-w>.
- (47) Pokle, A.; Ahmed, S.; Schweidler, S.; Bianchini, M.; Brezesinski, T.; Beyer, A.; Janek, J.; Volz, K. In Situ Monitoring of Thermally Induced Effects in Nickel-Rich Layered Oxide Cathode Materials at the Atomic Level. *ACS Appl. Mater. Interfaces* **2020**, *12* (51), 57047–57054. <https://doi.org/10.1021/acsami.0c16685>.
- (48) Yang, Z.; Ong, P.-V.; He, Y.; Wang, L.; Bowden, M. E.; Xu, W.; Droubay, T. C.; Wang, C.; Sushko, P. V.; Du, Y. Direct Visualization of Li Dendrite Effect on LiCoO₂ Cathode by In Situ TEM. *Small* **2018**, *14* (52), 1803108. <https://doi.org/10.1002/sml.201803108>.
- (49) Ong, P.-V.; Yang, Z.; Sushko, P. V.; Du, Y. Formation, Structural Variety, and Impact of Antiphase Boundaries on Li Diffusion in LiCoO₂ Thin-Film Cathodes. *J. Phys. Chem. Lett.* **2018**, *9* (18), 5515–5520. <https://doi.org/10.1021/acs.jpcclett.8b02185>.
- (50) Hasegawa, G.; Kuwata, N.; Tanaka, Y.; Miyazaki, T.; Ishigaki, N.; Takada, K.; Kawamura, J. Tracer Diffusion Coefficients of Li + Ions in c -Axis Oriented Li_xCoO₂ Thin Films Measured by Secondary Ion Mass Spectrometry. *Phys. Chem. Chem. Phys.* **2021**. <https://doi.org/10.1039/D0CP04598E>.
- (51) Nellist, P. D. The Principles of STEM Imaging. In *Scanning Transmission Electron Microscopy: Imaging and Analysis*; Pennycook, S. J., Nellist, P. D., Eds.; Springer-Verlag: New York, 2011.
- (52) Pennycook, S. J. Z-Contrast Stem for Materials Science. *Ultramicroscopy* **1989**, *30* (1), 58–69. [https://doi.org/10.1016/0304-3991\(89\)90173-3](https://doi.org/10.1016/0304-3991(89)90173-3).
- (53) Kilaas, R. Optimal and Near-Optimal Filters in High-Resolution Electron Microscopy. *J. Microsc.* **1998**, *190* (1–2), 45–51. <https://doi.org/10.1046/j.1365-2818.1998.3070861.x>.
- (54) Graaf, S. de; Momand, J.; Mitterbauer, C.; Lazar, S.; Kooi, B. J. Resolving Hydrogen Atoms at Metal-Metal Hydride Interfaces. *Sci. Adv.* **2020**, *6* (5), eaay4312. <https://doi.org/10.1126/sciadv.aay4312>.
- (55) Courtney, T. H. *Mechanical Behavior of Materials: Second Edition*; Waveland Press, 2005.

- (56) Shukla, A. K.; Ophus, C.; Gammer, C.; Ramasse, Q. Study of Structure of Li- and Mn-Rich Transition Metal Oxides Using 4D-STEM. *Microsc. Microanal.* **2016**, *22* (S3), 494–495. <https://doi.org/10.1017/S1431927616003329>.
- (57) Lee, H.-S.; Park, C.; Oh, C.-S.; Lee, H.-S.; Seo, H.; Hyun, Y.-T.; Lee, D.-W. Atomic Structure and Defect Energetics of LiCoO₂ Grain Boundary. *Mater. Res. Bull.* **2016**, *82*, 81–86. <https://doi.org/10.1016/j.materresbull.2016.04.017>.
- (58) Xiao, P.; Shi, T.; Huang, W.; Ceder, G. Understanding Surface Densified Phases in Ni-Rich Layered Compounds. *ACS Energy Lett.* **2019**, *4* (4), 811–818. <https://doi.org/10.1021/acseenergylett.9b00122>.
- (59) Mukherjee, P.; Lu, P.; Faenza, N.; Pereira, N.; Amatucci, G.; Ceder, G.; Cosandey, F. Atomic Structure of Surface-Densified Phases in Ni-Rich Layered Compounds. *ACS Appl. Mater. Interfaces* **2021**. <https://doi.org/10.1021/acsaami.1c00143>.
- (60) Su, Y.; Zhang, Q.; Chen, L.; Bao, L.; Lu, Y.; Shi, Q.; Wang, J.; Chen, S.; Wu, F. Riveting Dislocation Motion: The Inspiring Role of Oxygen Vacancies in the Structural Stability of Ni-Rich Cathode Materials. *ACS Appl. Mater. Interfaces* **2020**, *12* (33), 37208–37217. <https://doi.org/10.1021/acsaami.0c10010>.
- (61) Gong, Y.; Chen, Y.; Zhang, Q.; Meng, F.; Shi, J.-A.; Liu, X.; Liu, X.; Zhang, J.; Wang, H.; Wang, J.; Yu, Q.; Zhang, Z.; Xu, Q.; Xiao, R.; Hu, Y.-S.; Gu, L.; Li, H.; Huang, X.; Chen, L. Three-Dimensional Atomic-Scale Observation of Structural Evolution of Cathode Material in a Working All-Solid-State Battery. *Nat. Commun.* **2018**, *9* (1), 3341. <https://doi.org/10.1038/s41467-018-05833-x>.
- (62) Wang, C.; Han, L.; Zhang, R.; Cheng, H.; Mu, L.; Kisslinger, K.; Zou, P.; Ren, Y.; Cao, P.; Lin, F.; Xin, H. L. Resolving Atomic-Scale Phase Transformation and Oxygen Loss Mechanism in Ultrahigh-Nickel Layered Cathodes for Cobalt-Free Lithium-Ion Batteries. *Matter* **2021**. <https://doi.org/10.1016/j.matt.2021.03.012>.
- (63) Schweidler, S.; de Biasi, L.; Hartmann, P.; Brezesinski, T.; Janek, J. Kinetic Limitations in Cycled Nickel-Rich NCM Cathodes and Their Effect on the Phase Transformation Behavior. *ACS Appl. Energy Mater.* **2020**, *3* (3), 2821–2827. <https://doi.org/10.1021/acsaem.9b02483>.
- (64) Schweidler, S.; de Biasi, L.; Garcia, G.; Mazilkin, A.; Hartmann, P.; Brezesinski, T.; Janek, J. Investigation into Mechanical Degradation and Fatigue of High-Ni NCM Cathode Material: A Long-Term Cycling Study of Full Cells. *ACS Appl. Energy Mater.* **2019**, *2* (10), 7375–7384. <https://doi.org/10.1021/acsaem.9b01354>.
- (65) HRTEM Filter http://www.dmscripting.com/hrtem_filter.html (accessed 2021 -02 -01).
- (66) Hÿtch, M. J.; Snoeck, E.; Kilaas, R. Quantitative Measurement of Displacement and Strain Fields from HREM Micrographs. *Ultramicroscopy* **1998**, *74* (3), 131–146. [https://doi.org/10.1016/S0304-3991\(98\)00035-7](https://doi.org/10.1016/S0304-3991(98)00035-7).

(67) Useful Plugins and Scripts for DigitalMicrograph —
Strukturforschung/Elektronenmikroskopie https://www.physik.hu-berlin.de/en/sem/software/software_frwrtools (accessed 2021 -02 -01).